Vrije Universiteit Brussel

VRIJE
UNIVERSITEIT
BRUSSEL

Effect of Heat Treatments on the Anodizing Behavior of Additive Manufactured AlSi10Mg

Rubben, Tim; Revilla, Reynier I.; De Graeve, Iris

Document Version:
Accepted author manuscript

[Link to publication](#)

Effect of heat treatments on the anodizing behavior of additive manufactured AlSi10Mg.

Tim Rubben,[z] Reynier I. Revilla, and Iris De Graeve

Vrije Universiteit Brussel (VUB), Dept. of Chemistry and Materials, Research Group of Electrochemical and Surface Engineering (SURF), Pleinlaan 2, 1050 Brussels, Belgium
[z]E-mail: trubben@vub.be

Abstract

In this work, the effect of heat treatments on the anodizing behavior of additive manufactured AlSi10Mg material is studied. Specimens are subjected to artificial aging or stress release heat treatments, followed by galvanostatic anodizing in sulfuric acid. Optical and scanning electron microscopy are employed to study the microstructure and the oxide layer characteristics. Upon applying the heat treatments, the microstructure shows a gradual evolution from a continuous 3D silicon network towards separate coarse silicon particles in an aluminum matrix. The morphology of the silicon phase is found to be a deciding factor as it determines the fraction of silicon that is oxidized during anodizing. This in turn is found to have a direct impact on the anodizing efficiency and oxide layer uniformity. Thicker and more uniform oxide layers are obtained for the additive manufacture AlSi10Mg specimens after the silicon network is broken up due to the heat treatments.

1. Introduction

Selective laser melting (SLM) is an additive manufacturing technique in which parts are produced layer by layer by selective melting of a pattern in a powder bed[1]. A high power laser is used to deliver the heat necessary for melting. As the layers are molten on top of each other, they are effectively welded together and a dense part is created[2]. This study focuses on AlSi10Mg specimens produced by SLM. As a cast alloy, the AlSi10Mg alloy is widely used in the automotive, aerospace and domestic industries due to its good castability, weldability, hardenability and corrosion resistance[3,4]. Since the alloy has a near eutectic composition, the melting range (600-555°C) is reduced compared to pure aluminum (660°C). This increases weldability and facilitates the processing with laser based techniques such as SLM. Furthermore, it allows simultaneous solidification of all phases, improving resistance against thermal cracking.

During the SLM process, the material is rapidly molten and resolidified[5]. This enables the formation of a very fine microstructure[3,6] but also induces thermal stresses into the material[7]. Due to the movement of the heat source, the solidification time varies over the melt pool. It is lowest at the centerline and increases when going to the edge of the melting track[4,8]. This leads to a differential in thermal compression, giving residual stresses[9]. These can induce warpage and reduce the fatigue resistance of the material. To prevent this, stress release heat treatments are commonly performed to reduce the residual stresses[10,11].The presence of magnesium in the alloy makes it susceptible to another heat treatment, artificial aging. It enables the formation of Mg_2Si precipitates, hardening the material[3]. Nevertheless, to the best of our knowledge, the actual formation of Mg_2Si precipitates has not been demonstrated yet in AM Al alloys. As the rapid solidification during fabrication ensures that a large fraction of the alloying elements is in solution, no solution treatment

needs to be performed before the artificial aging. This has as a benefit that the fine microstructure, giving good mechanical properties to the material, is not destroyed[8].

Several papers[4,6,7,12,13] have been written on the microstructure of additive manufactured AlSi10Mg. The microstructure consists of aluminum cells surrounded by a fibrous silicon network. At the center of the melt pool the Al cells are smallest, giving very fine features. They increase in size towards the melt pool borders, where the solidifying time was longer, resulting in a more coarse cellular structure. Because of the larger cell size, the melt pool borders can be distinguished at a macroscopic scale[4]. Next to the melt pool border a region exists where the silicon network has broken up into idiomorphic particles. This region has been identified in previous works as a heat affected zone (HAZ) and is created when the material is affected by the heat of the laser passing and creating the adjacent melt pool[4]. Upon heat treatment, the material progressively approaches its equilibrium. This leads to a collapse of the silicon network and microstructure ripening, changing the size, morphology and distribution of the silicon phase[13,14]. In a previous study[20] the effect of artificial aging and stress release heat treatments on the microstructure was investigated. It was found that artificial aging at 170°C for 6h (AA170) did not have a significant impact on the microstructure. Stress releases at 250°C (SR250) and 300°C (SR300) for 2h on the other hand were found to lead to a (partial) breakup of the silicon network into separate coarse particles. In this work these specimens are anodized in order to investigate the influence of the evolved microstructure on the anodizing behavior.

Aluminum and its alloys have an inherent protection against atmospheric corrosion due to the presence of a protective oxide film that forms spontaneously and immediately in air. This natural oxide film is however limited in thickness, a typical value for the thickness is 2.5 nm[15]. Anodizing or anodic oxidation is an electrolytic process that enables the production of much thicker oxide coating, improving properties like abrasion resistance, electrical insulation, adhesion and corrosion resistance[15]. Previous research[16,17] has pointed out that additive manufactured and cast alloy material shows different anodizing behavior. Higher anodizing voltages, lower oxide growth rates and a smoother oxide film were obtained for the additive manufactured specimens. These differences were found to depend on the distribution of silicon, the cast alloy having large dendritic structures while the AM specimen has a fine distribution in a 3D network[16]. During anodizing, the silicon of the AM materials is completely oxidized, unlike the silicon in the cast alloy which is only superficially oxidized[17]. This is related to the size of the silicon inclusions. As presented by Zhu et al[18] for a cast alloy, a larger fraction of silicon is oxidized in Al-Si alloys when the precipitates are smaller. Since the morphology of the silicon phase plays an important role in the anodizing process, it is expected that the microstructure evolution induced by the heat treatments will have an effect on the anodizing behavior as well. To study this, galvanostatic anodizing in sulfuric acid solution is performed and the produced oxide layers are investigated using optical microscopy and SEM.

2. Experimental

2.1 Specimens

A ProX DMP 320 machine was used to fabricate the AM specimens from LaserForm AlSi10Mg powder by selective laser melting. The process utilized a laser with a power of 500 W to generate a laser energy density of 51 J/mm^3 for the specimen preparation. The process was executed in an

argon atmosphere, resulting in an oxygen content below 50 ppm. Aleris provided the cast aluminum alloy (AA4420) that was used as a reference material. Three types of heat treatments were performed on the AM specimens. A first treatment is an artificial aging treatment at 170°C for 6 hours (AA170). The second treatment is a stress release treatment at 300°C for 2 hours (SR300). For the third treatment a more moderate temperature was chosen for the stress release treatment, performed at 250°C for 2 hours (SR250). All the specimens were mechanically ground and polished, finishing with 0,04 µm standard colloidal silica suspension (OP–S). The chemical specification of the metal powder used is given in Tables

Table 1, as is the chemical composition of the cast alloy.

2.2 Anodizing procedure

Galvanostatic anodizing with a current density of 10 mA/cm^2 was carried out in a stirred 3M H$_2$SO$_4$ solution at room temperature. An ES 0300-0.45 power supply from Delta Elektronika was used. To measure the anodic potential, a two electrode cell configuration was used with the specimen acting as the working electrode and a platinum electrode as the counter electrode. Before anodizing, the specimens were ultrasonically cleaned in acetone and ethanol, each with an immersion time of 3 minutes. After the anodizing, the specimens were rinsed with distilled water and dried with an air stream.

2.3 Sample characterization

The various specimens were characterized by using optical microscopy and scanning electron microscopy. In order to study the microstructure before anodizing, polished specimens were etched using Keller's reagent. The optical microscope images were obtained at several magnifications using a Leitz Metallovert optical microscope. A FE-SEM JEOL JSM–7100F was used to take SEM images with a 15 kV acceleration voltage, a 5 pA probe current and a working distance of 10 mm. To get a better contrast between different elements, images showing the cross-section of the oxide layer were taken in backscattered electron mode.

3. Results

3.1 Microstructure characterization

Prior to anodizing, microstructure characterization was performed using optical microscopy and scanning electron microscopy. The results most relevant for the current study are given here. The microstructure evolution was discussed in more depth in a previous work[20] . Figure 1 shows optical micrographs that reveal the surface of non heat treated (NHT) specimens that were polished in the plane perpendicular (XY) to the building direction (Figure 1a) and the plane parallel (XZ) to the building direction (Figure 1b). The melt pool borders from the laser source can be clearly seen. There, the microstructure is coarser, making it possible to distinguish them at a macroscopic scale[4]. Overlapping melt pools of subsequent layers can be observed in the XZ plane, while elongated tracks are found in the XY plane. These elongational tracks have different shapes and sizes as the cross-section cuts through the melt pools at different places resulting in varying widths[7].

Higher magnification images were obtained using SEM. These can be used to show the effect of the heat treatments on the microstructure. Figure 2 shows the polished surface of XY specimens

before and after application of one of the heat treatments. Similar results were obtained for the XZ specimens. Melt pool borders are indicated by the discontinuous lines. Figure 2a shows the surface of a NHT specimen. It shows cellular aluminum cells surrounded by a relatively continuous fibrous eutectic silicon network. A coarser microstructure with larger cell sizes is noted at the melt pool borders. Right outside the melt pool border, in the heat affected zone, the cellular network has coarsened into separate idiomorphic silicon particles. Figure 2b shows the surface of an AA170 specimen. It has a microstructure that is very similar to that of the NHT specimen. On the other hand, the stress releases have a more profound impact on the microstructure. Upon applying the SR250 heat treatment, the silicon network gets disturbed and starts to break up into separate precipitates (see Figure 2c). The network is still largely continuous but has become disconnected at several spots. When the temperature of the stress release is increased to 300°C (SR300), the breakdown of the silicon network is more complete. This is visible in Figure 2d, where it is shown that the silicon network has been broken up into separate, coarse precipitates. Regardless of the applied heat treatment, larger silicon phases are retained at the melt pool borders. To summarize, upon application of the different heat treatments the microstructure shows an evolution from a continuous fibrous silicon network (NHT and AA170) to a partially broken network (SR250) and then to separate, coarse silicon precipitates (SR300).

3.2 Potential vs time behavior

A representative selection of anodizing curves is given in Figure 3a. It contains anodizing data for AM specimens before and after application of a heat treatment. Data for a cast alloy, taken from the research performed by Revilla et al.[16], was added as a reference. Only data obtained during anodizing of the surface perpendicular to the building direction (XY) are shown. Similar trends were obtained for surfaces parallel to the building direction (XZ). Large changes in final voltage are noted, being lowest for the cast alloy and highest for the AM NHT and AM AA170 specimens. The final voltage of the AM specimen drops on applying the higher temperature stress releases. After the SR250 treatment a large drop in final voltage is observed. If the temperature of the stress release is increased to 300°C, the voltage drop is even larger. The anodizing behavior of the stress released specimen is getting closer to the one seen for CA specimen.

A closer look at the initial stage of anodizing is given in Figure 3b. The CA specimen shows the typical behavior for barrier growth followed by pore development. First a sharp linear increase corresponding to linear growth of the oxide layer before pore initiation, followed by a quick progression to a steady state. The various AM specimens deviate from this behavior. The initial linear increase is similar for all specimens but steady state is reached later and at higher voltage than for the CA specimen. The AA170 and NHT specimens only reach steady state after about 300 s of anodizing time. The time before reaching steady state decreases with heat treatment temperature, taking about 200 s for the SR250 specimen and about 80 s for the SR300 specimen.

Figure 4 gives the anodizing curves for surfaces perpendicular (XY) and parallel (XZ) to the building direction. The XZ specimens show the same trend in final voltage as the XY specimens. The NHT and AA170 specimens reach the highest voltage while the final voltage of the stress released specimens decreases with increasing temperature of the heat treatment. The NHT and AA170 specimens show a large difference in final voltage between the XY and XZ surfaces, with the surface perpendicular to the building direction (XY) reaching higher voltages. This has been

previously observed for NHT specimens[16]. The difference was explained by the XY plane having smaller aluminum cell size, causing more of the aluminum to be in the vicinity of silicon and increasing the anodizing voltage. For the stress released specimens this difference has become much smaller.

A certain spread in the data is observed for replicated experiments. This is illustrated in Figure 5. Despite this spread, a clear trend in anodizing voltage can be seen: AA170 > SR250 > SR300. A large spread in data is found for the AA170 specimens, as also observed for NHT specimens in an earlier work[16]. The SR250 specimens show a much more limited spread while the SR300 specimens show almost no spread. This can be attributed to small changes in the plane which is polished. As was seen in Figure 4, there is a difference in final anodizing voltage between the XY and XZ surfaces of NHT and AA170 specimens. Now, when an XY specimen is polished, there is an error in the polishing angle and the polishing will not be perfectly in the XY plane; as such after polishing there is some deviation towards the XZ plane. Hence, these surfaces are then not purely XY anymore resulting in a spread in the anodizing data. The same reasoning can be applied to the XZ specimens. In the case of the SR250 and SR300 specimens, which do not show such a large variation in microstructure between XY and XZ, this polishing error is less critical, explaining why there is no large spread in anodizing data.

3.3 Anodic oxide layer thickness

Previous research[16,17] has pointed out that the morphology of silicon plays an important role in determining the oxide growth rate and uniformity. Because the heat treatments induce a significant microstructure evolution, it is expected that the anodic oxide layer will be affected. As such, the oxide layer was investigated using optical microscopy. Figure 6 shows optical microscopy images of the cross-section of anodized specimens. The XY surface of each of the shown specimens was anodized for 1200s. Differences in thickness and uniformity of the oxide layers can be observed. The thickest oxide layer is achieved with the cast alloy. However, it can be seen that the oxide layer is locally affected by the presence of large silicon precipitates, causing a drastic reduction in oxide layer thickness as was observed in a previous work[16]. Concerning the AM specimens, the AA170 specimen appears to have the thinnest and least uniform layer. The stress released specimens appear to be thicker and more uniform, with the SR300 specimen showing the thickest and most uniform layer for an AM specimen. To have more quantitative data on the evolution of thickness and uniformity, besides the optical microscopy pictures, a statistical analysis was performed. To achieve this, the thickness was measured at various spots and the average and standard deviation were determined (To obtain this, 7 to 10 areas equally spaced in the specimen were chosen. In each area 20 points were measured, each spaced 20μm apart). The results of this are presented in Figure 7 and Figure 8, respectively showing the average thickness and the relative standard deviation (standard deviation of the thickness divided by the average oxide thickness) of the specimens. The data for the cast alloy and NHT material were taken from the research performed by Revilla et al[16].

The evolution of the average thickness of the various specimens with the anodizing time is shown in Figure 7. The slope of these curves is a measure of the anodizing rate. The large difference in thickness between the cast alloy and NHT AM material was previously discussed by Revilla et al[16]. The AA170 specimen shows a behavior that is very similar to the NHT AM material. The two curves almost superimpose. The stress released AM material on the other hand shows a behavior

that lies between that of the cast alloy and that of the NHT AM material. The higher the temperature of the stress release, the thicker the obtained oxide layer for a given anodizing time and thus the closer the anodizing rate gets to that of the cast alloy. Figure 8 shows the relative standard deviation (RSD) on the thickness of the AM material for various anodizing times. The RSD is used instead of the standard deviation as it gives an improved measure of the uniformity. The NHT AM material shows the highest deviation, thus it has the least uniform oxide layer. For the stress released materials lower deviations are found, with the specimens stress released at 300°C having the lowest RSD. For the heat treatments studied in this work, anodizing produces thicker and more uniform oxide layers after heat treatment at higher temperatures.

Table 2 summarizes the oxide growth rates for the various specimens. They were calculated from the linear fitting of the data shown in Figure 7. A general trend can be observed. Higher growth rates are obtained when less of the aluminum is positioned in the immediate vicinity of silicon. As such, the obtained thickness after a certain anodizing time will be greater. A trend on uniformity can also be noted. Lower standard deviations are obtained for AM specimens where the silicon network is more broken up. This corresponds with what is seen in Figure 8. These values were used to calculate a relative anodizing efficiency by dividing the growth rate of the specimens by the growth rate of the cast alloy, as shown in Figure 9. The relative anodizing efficiency of the AM specimens gradually increases when the heat treatments break up the silicon network to a greater extend, finally reaching 69% compared to that of the cast alloy.

3.4 Characterization of anodic oxide layer

Figure 10 shows backscattered electron images of the cross-section surface of a NHT specimen that was anodized for 1200 s. In Figure 10a the formed oxide layer is clearly distinguishable. The oxygen, which has a lower atomic number than silicon or aluminum, darkens the response. It is possible to distinguish the cells of the cellular Si network. The Si inside the oxide layer has darkened considerably compared to the Si visible outside the oxide layer which has a much brighter appearance. Zhu et al[18] described for cast aluminum the split of a partially oxidized Si particle in a dark and light response. They identified the dark response as being silicon oxide and the light response as being elemental Si. It thus appears that the Si in the oxide layer has been almost completely oxidized. Some smaller bright spots are visible. They could indicate that a very small fraction of the material remains unoxidized but are thought to result from the polishing procedure. Regardless, for a NHT specimen most of the silicon in the oxide layer is oxidized as has been recently demonstrated by XPS analysis[17]. The border between oxide layer and unoxidized material has an irregular appearance. At several places the border seems to match the cellular morphology of the Si network.

In Figure 10b a higher magnification of the region indicated by the square in Figure 10a is visible. In the region indicated by the circle it can be more clearly seen that the border matches the cellular silicon network. The border coincides with the dark response of the silicon oxide that is found at the edge of the cells. At this magnification the pores resulting from anodizing are visible inside the cells. They go down alongside the length of the cell but show a branching behavior as was also seen in a previous work[16]. The direction of the pores is reoriented towards the Si of the cellular

boundary. The orientation of the pores of one cell does not seem to influence the pores of adjacent cells, the silicon appears to act as a sort of boundary. This can be most clearly seen at the top of the figure. After passing the silicon, the orientation of the pores is normal to the silicon phase.

Figure 11 shows backscattered electron images of the cross-section surface of a SR300 specimen that was anodized for 1200 s. Figure 11a shows the oxide layer with embedded Si particles. The border between oxide layer and unoxidized material has a somewhat more uniform appearance, though it is locally perturbed in the vicinity of Si particles. Several Si particles are visible. For the larger particles two regions can be denoted; a light part at the bottom and a darker response on top. The dark part most likely corresponds to silicon oxide and the lighter part corresponds to elemental Si[18]. In contrast to the NHT material, the Si is now only partially oxidized. Some of the smaller Si particles have a completely dark appearance indicating that they are completely oxidized. In Figure 11b a higher magnification of the region indicated by the square in Figure 11a is visible. The bottommost circle shows the perturbation of the border due to the presence of a Si particle, showing that the oxide front has not progressed as far as it does when it is farther away from any Si particles. In the uppermost circle one of the partially oxidized Si particles can be observed. The thickness of the oxidized part of this and other partially oxidized Si particle appears to be about 100 nm.

There may be some ambiguity as to whether the dark response in Figure 11 corresponds to silicon oxide or to cavities. To clarify this Figure 12 can be used. It shows a partially oxidized silicon particle at a higher magnification. The light and dark responses show a clear continuity, indicating that the dark response is silicon oxide. At the top of the particle some small cavities giving a much darker response can be seen. Between the particles, the pores resulting from the anodizing can be seen. The pores go down with minor branching unless they pass a Si particle. If the pore has a Si particle right beneath it, partial oxidation occurs but the pores do not propagate through the Si[19]. If the pore passes to the left or right of a Si particle, it is deviated or splits towards it. In most cases it does not reach the Si phase but it instead meets other pores beneath the Si particle. As this happens multiple times, a trace appears below the Si.

4. Discussion

The heat treatments have a large influence on the anodizing behavior of AM AlSi10Mg alloy. The reason for the differences in anodizing behavior after application of various heat treatments is found in the corresponding changes in microstructure. It is seen that the silicon plays a crucial role in the anodizing behavior. The different specimens all have the same silicon content so it is the morphology of the silicon phase that causes the different anodizing behaviors. During anodizing, silicon is anodized at a lower rate than aluminum[18]. In addition, the silicon is more resistive than the adjacent aluminum matrix[19]. Hence if silicon is being anodized, the oxide growth rate will be lower and the anodizing voltage will be higher. The larger the fraction of silicon that is anodized, the larger this effect will become.

The difference between the cast alloy and NHT AM specimens was previously explained by Revilla et al[16].They found that the voltage-time response and oxide film characteristics were significantly affected by the unique microstructure produced by AM. This was linked to the distribution of silicon, having large dendritic structures for the cast alloy and a fine distribution for the AM specimen. For the fine distribution it was demonstrated that a larger fraction of the charge is

consumed by the silicon, giving lower film growth rate. An anisotropic behavior was found for the AM specimens. The final voltage of the voltage-time curve was found to be higher for surfaces oriented in the XY direction than in the XZ direction. An explanation for this behavior was found in differences in the aluminum cell size. For surfaces oriented in the XY plane these cells are smaller, causing a higher fraction of the aluminum to be affected by the proximity to silicon.

A similar discussion can be made for the various heat treated AM specimens, with the anodizing behavior depending on how the microstructure was affected. When the silicon network remains continuous, such as is the case for the NHT and AA170 specimens, it acts as a barrier against the propagation of the oxide front. Therefore, the silicon will be almost completely anodized. This was observed for the NHT specimen in Figure 10, where only the darker response corresponding to silicon oxide was seen in the oxide layer while the lighter response of unoxidized elemental silicon was observed below the oxide layer. As most of the silicon is anodized, the obtained anodizing efficiency will be the lowest (see Figure 9), resulting in thin oxide layers. Furthermore, the anodizing voltage will reach the highest values (see Figure 3). As a result of the differences in aluminum cell size between the XY and XZ surfaces, an anisotropy exists in final anodizing voltage. The anisotropy was previously described by Revilla et al[16] for the NHT specimens and is again observed for the AA170 specimens as the artificial aging treatment has not significantly changed the microstructure.

The stress release heat treatments have a more profound impact on the microstructure of the AM material. They cause a break-up of the silicon network into separate precipitates. The more broken the silicon network is, the lower is the resistance to anodizing, as the oxide front can more easily circumvent the silicon. Because the oxide front does not need to move through the silicon, a smaller fraction of the silicon facing the oxide front will be anodized. This is visible in Figure 11 and Figure 12 for the SR300 specimen. The silicon particles in the oxide layer show a dark response at the top compared to a lighter response at the bottom. Below the oxide layer, the silicon particles only show a light response, indicating again that the dark response is silicon oxide. The oxidized part of the silicon particles was found to be of similar thickness, regardless of particle size. As a consequence, smaller particles are completely oxidized while larger particles are only partially oxidized. This means that if the silicon precipitates are of larger dimensions, a lower fraction of the silicon will be anodized. Similar observations about the effect of the size of the silicon particles were previously made by Zhu et al[18] for a cast alloy. As a lower fraction of the silicon is anodized, the stress released specimens have a lower anodizing voltage (see Figure 3) and a higher anodizing efficiency (see Figure 9) than the specimens with a continuous silicon network, resulting in thicker oxide layers. The anisotropy in anodizing voltage between the XY and XZ surfaces is no longer observed. This is a result of the microstructure having become spatially more uniform and independent of the building direction after stress release heat treatment, reducing the differences between the different planes. Moreover, the influence of silicon on the anodizing voltage diminishes as a lower fraction of the silicon is oxidized, reducing the anisotropic behavior further.

A differentiation can be made between the stress released specimens. For the SR250 specimens the silicon network is only partially broken whereas for the SR300 specimens the silicon network is broken more thoroughly. In the SR250 specimen most of the aluminum is still in the vicinity and thus in the sphere of influence of silicon. This increases the anodizing voltage and decreases the

oxide growth rate compared to the SR300 specimen. For the SR300 specimen the phase separation between aluminum and silicon occurs to a greater extend, so a smaller fraction of the aluminum is affected by the silicon and the anodizing voltage will be lower. The cast alloy can be seen as a more extreme case of the SR300 specimen, where the aluminum and silicon are phase separated to an even greater extent (see Figure 6d). Because of this, the moving oxide front does not encounter silicon in a large part of the material. This highly reduces the impact of the silicon, giving the lowest anodizing voltage and the highest oxide growth rates. A side note should be made for the cast alloy: it was previously reported that in the vicinity of the dendritic silicon the thickness of the obtained oxide layer is significantly decreased[16]. This can also be seen in Figure 6d. In the end, the final anodizing voltage measurement shows the following order: NHT ≈ AA170 > SR250 > SR300 > Cast alloy (Figure 3) and the oxide growth rate follows the order of Cast alloy > SR300 > SR250 > AA170 ≈ NHT (see Table 2).

Another point of interest is the transition to a stable regime in the voltage-time curve (see Figure 3b). After 10 seconds the slope drastically changes, until it stabilizes after a certain time. This transition seems to depend on the applied heat treatment. The AM specimens show a much larger transition region than the cast alloy. Previous research[17] on NHT specimens has pointed out that the time interval of the transition region corresponds with the time required to oxidize one cell. A similar behavior is now found for the stress released specimens. By taking into account the oxide growth rate (see

Table 2) of SR300 and the time interval of the transition region (≈50 s), a match is found between the size of a silicon particle (≈200 nm) and the oxide layer thickness at time of stabilization. As a large part of the silicon is oxidized, a steady state is reached when the oxide layer thickness approaches the average size of the silicon features[17]. This clearly indicates that the morphology of the silicon determines this transition behavior.

Aside from the oxide growth rate, the uniformity of the obtained oxide layer is of importance. The relative standard deviation of the various specimens is given in Figure 8. It can be used as a measure of uniformity, taking into account the varying oxide layer thicknesses of the specimens. An apparent order in uniformity is identified: NHT < AA170 < SR250 < SR300. The morphology of the silicon is again the deciding factor. The presence of silicon impedes the growth of the oxide layer as it consumes part of the charge, reducing the anodizing efficiency. Its influence on the oxide layer can be seen in Figure 10 for the NHT specimen and in Figure 11 for the SR300 specimen. It is seen that the metal/oxide interface progresses less far near silicon. For the NHT and AA170 specimens most of the silicon is oxidized, reducing the overall oxide layer thickness. Previous research[17] has pointed out that the melt pool borders of NHT material contains a slightly higher silicon content, locally reducing the oxide layer thickness and decreasing the uniformity. This gives a distribution in thickness, visible qualitatively in Figure 6 and quantitatively in Figure 8. The stress released specimens can be seen to be more uniform. A reason for this is that a lower fraction of the silicon is anodized, reducing the local thinning effect that leads to a decrease in uniformity. Another contribution might be that there is a more even distribution of the silicon. Therefore, the moving oxide front will be less affected and the oxide layer will be more uniform.

5. Conclusion

- Differences in anodizing behavior were observed for the different specimens. Heat treated specimens can be anodized but their behavior was found to depend on how the morphology of the silicon phase was affected. In the case of a continuous silicon network, most of the silicon will be oxidized. This is representative for the non heat treated (NHT) and artificially aged (AA170) specimens. When the microstructure consists of separate precipitates, only a fraction of the silicon facing the oxide front will be oxidized. This is the case for the stress released specimens (SR250 and SR300). The differences in fraction of silicon anodized were used to explain the differences in behavior between the various specimens.

- The specimens showed a varied voltage-time response during anodizing. The cast alloy used as a reference showed the typical steady state growth while the AM specimens had an increase in voltage for longer times before reaching a steady state at higher voltages. The final anodizing voltage was found to increase when higher fractions of silicon were anodized, giving the following order: NHT $\approx$ AA170 > SR250 > SR300 > cast alloy. The anodizing efficiency is affected as well, as it increased when lower fractions of silicon were anodized, giving the order: NHT < AA170 < SR250 < SR300 < cast alloy.

- The anisotropic behavior in anodizing voltage between the different building planes that was previously observed for the NHT material is again observed for the AA170. After stress release, this effect has diminished in importance due to a homogenization of the microstructure and a decrease in the fraction of silicon that is oxidized.

- The heat treatments were found to have an impact on the uniformity of the produced anodic oxide layer in AM AlSi10Mg specimens. When silicon is oxidized it leads to a decrease of the oxide growth rate. If there is a higher silicon content at a certain spot (e.g. at the melt pool border), this can lead to a local thinning effect. When most of the silicon is anodized this has a strong effect on the uniformity, as is the case for the NHT and AA170 specimens. For the stress released specimens less of the silicon is oxidized, diminishing the impact of the local thinning effect and improving the uniformity. This gives the following order in uniformity: NHT > AA170 > SR250 > SR300

References

1.   D. Herzog, V. Seyda, E. Wycisk, C. Emmelmann, Additive manufacturing of metals, Acta Mater. 117 (2016) 371–392.

2.   E. Louvis, P. Fox, C.J. Sutcliffe, Selective laser melting of aluminium components, J. Mater. Process. Tech. 211 (2011) 275–284.

3.   K. Kempen, L. Thijs, J. Van Humbeeck, J. Kruth, Mechanical properties of AlSi10Mg produced by Selective Laser Melting, Phys. Procedia. 39 (2012) 439–446.

4.   L. Thijs, K. Kempen, J. Kruth, J. Van Humbeeck, Fine-structured aluminium products with controllable texture by selective laser melting of pre-alloyed AlSi10Mg powder, Acta Mater. 61 (2013) 1809–1819.

5.   K.G. Prashanth, B. Debalina, Z. Wang, P.F. Gostin, A. Gebert, M. Calin, M. Kamaraj, S. Scudino, J. Eckert, Tribological and corrosion properties of Al – 12Si produced by selective laser melting, J. Mater. Res. 29 (2014).

6.   H. Asgari, C. Baxter, K. Hosseinkhani, M. Mohammadi, Materials Science & Engineering A On microstructure and mechanical properties of additively manufactured AlSi10Mg _ 200C using recycled powder, Mater. Sci. Eng. A. 707 (2017) 148–158.

7.   D. Manfredi, F. Calignano, M. Krishnan, R. Canali, From Powders to Dense Metal Parts: Characterization of a Commercial AlSiMg Alloy Processed through Direct Metal Laser Sintering, Materials (Basel). 6 (2013) 856–869.

8.   K. Kempen, L. Thijs, J. Van Humbeeck, J. Kruth, Processing AlSi10Mg by selective laser melting : parameter optimisation and material characterisation, Mater. Sci. Technol. 31 (2015) 917–923.

9.   J. Zhang, X. Wang, S. Paddea, X. Zhang, Fatigue crack propagation behaviour in wire + arc additive manufactured Ti - 6Al - 4V : Effects of microstructure and residual stress, JMADE. 90 (2016) 551–561.

10.   A. Benallal, Residual Stress Modelling During the Oil Quenching of an Astroloy Turbine Disk, Miner. Met. Mater. Soc. (1992) 73–82.

11.   K.G. Watkins, M.A. Mcmahon, W.M. Steen, Microstructure and corrosion properties of laser surface processed aluminium alloys : a review, Mater. Sci. Eng. A. 231 (1997) 55–61.

12.   C. Yan, L. Hao, A. Hussein, P. Young, J. Huang, Microstructure and mechanical properties of aluminium alloy cellular lattice structures manufactured by direct metal laser sintering, Mater. Sci. Eng. A. 628 (2015) 238–246.

13.   W. Li, S. Li, A. Zhang, Y. Zhou, W. Qingsong, C. Yan, Y. Shi, Effect of heat treatment on AlSi10Mg alloy fabricated by selective laser melting : Microstructure evolution ,

mechanical properties and fracture mechanism, Mater. Sci. Eng. A. 663 (2016) 116–125.

14. P. Yang, M.A. Rodriguez, L.A. Deibler, B.H. Jared, J. Griego, A. Kilgo, A. Allen, D.K. Stefan, Effect of thermal annealing on microstructure evolution and mechanical behavior of an additive manufactured AlSi10Mg part, J. Mater. Res. 33 (2018) 1701–1712.

15. J. Evertsson, F. Bertram, F. Zhang, L. Rullik, L.R. Merte, M. Shipilin, M. Soldemo, S. Ahmadi, N. Vinogradov, F. Carlà, J. Weissenrieder, M. Göthelid, J. Pan, A. Mikkelsen, J. Nilsson, E. Lundgren, The thickness of native oxides on aluminum alloys and single crystals, Appl. Surf. Sci. 349 (2015) 826–832.

16. R.I. Revilla, H. Terryn, I. De Graeve, Role of Si in the Anodizing Behavior of Al-Si Alloys: Additive Manufactured and Cast Al-Si10-Mg, J. Electrochem. Soc. 165 (2018) C532–C541.

17. R.I. Revilla, D. Verkens, L. Malet, L. Thijs, I. De Graeve, Galvanostatic Anodizing of Additive Manufactured Al-Si10-Mg Alloy St´, J. Electrochem. Soc. 164 (2017) 1027–1034.

18. B. Zhu, S. Seifeddine, P.O.Å. Persson, A.E.W. Jarfors, P. Leisner, C. Zanella, A study of formation and growth of the anodised surface layer on cast Al-Si alloys based on different analytical techniques, JMADE. 101 (2016) 254–262.

19. L.E. Fratila-apachitei, H. Terryn, P. Skeldon, G.E. Thompson, J. Duszczyk, L. Katgerman, Influence of substrate microstructure on the growth of anodic oxide layers, Electrochim. Acta. 49 (2004) 1127–1140

20. T. Rubben, R.I. Revilla, I. De Graeve. Influence of heat treatments on the corrosion mechanism of additive manufactured AlSi10Mg. Accepted by *Corrosion Science* (2018).

Tables

Table 1: Specifications of the chemical composition of the LaserForm AlSi10Mg powder used to fabricate the specimens (AM) and of the AA4420 cast alloy (CA).

	Chemical composition (wt%)										
	Ti	Sn	Pb	Zn	Ni	Mn	Cu	Fe	Mg	Si	Al
AM	<0.15	<0.05	<0.05	<0.10	<0.05	<0.35	<0.10	<0.55	0.20-0.45	9.00-11.00	Rest
CA	-	-	-	<0.18	-	<0.09	<0.07	<0.38	0.5-0.7	9.48-9.89	Rest

Table 2: Oxide growth rate during anodizing of different specimens (In 3M H_2SO_4 electrolyte and with a current density of 10 mA/cm^2.)

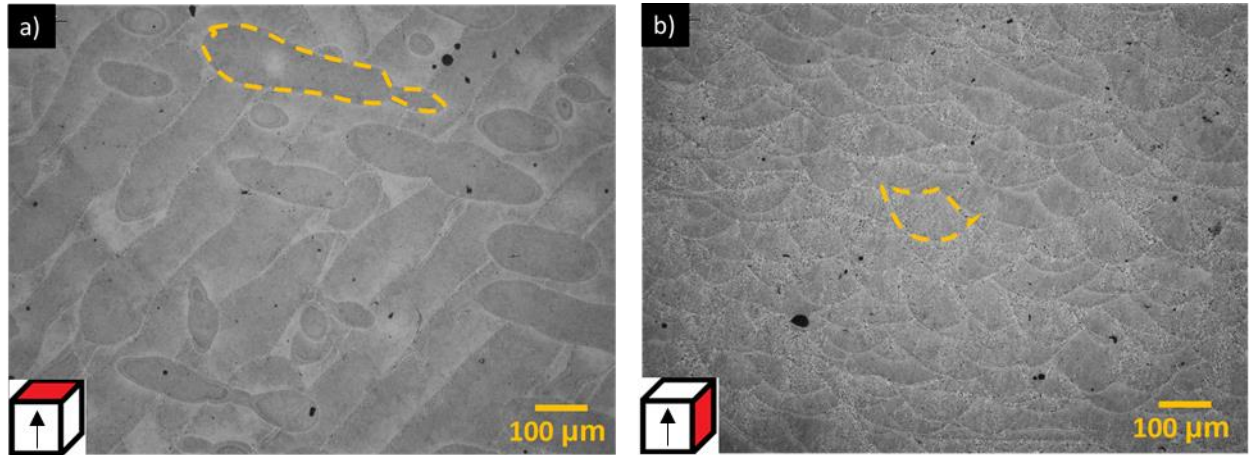| Oxide growth rate (µm/min)				
NHT	AA170	SR250	SR300	Cast Alloy
0,18 ± 0,02	0,21 ± 0,02	0,23 ± 0,01	0,26 ± 0,01	0,37 ± 0,03

Figures

Figure 1: Optical images of the surface of AM material. a) Surface perpendicular to the building direction (XY) and b) surface parallel to the building direction (XZ). The cube shows the position of the surface plane (in red) in relation to the building direction (represented by the arrow). The borders of some of the melt pools are denoted by the discontinuous lines.
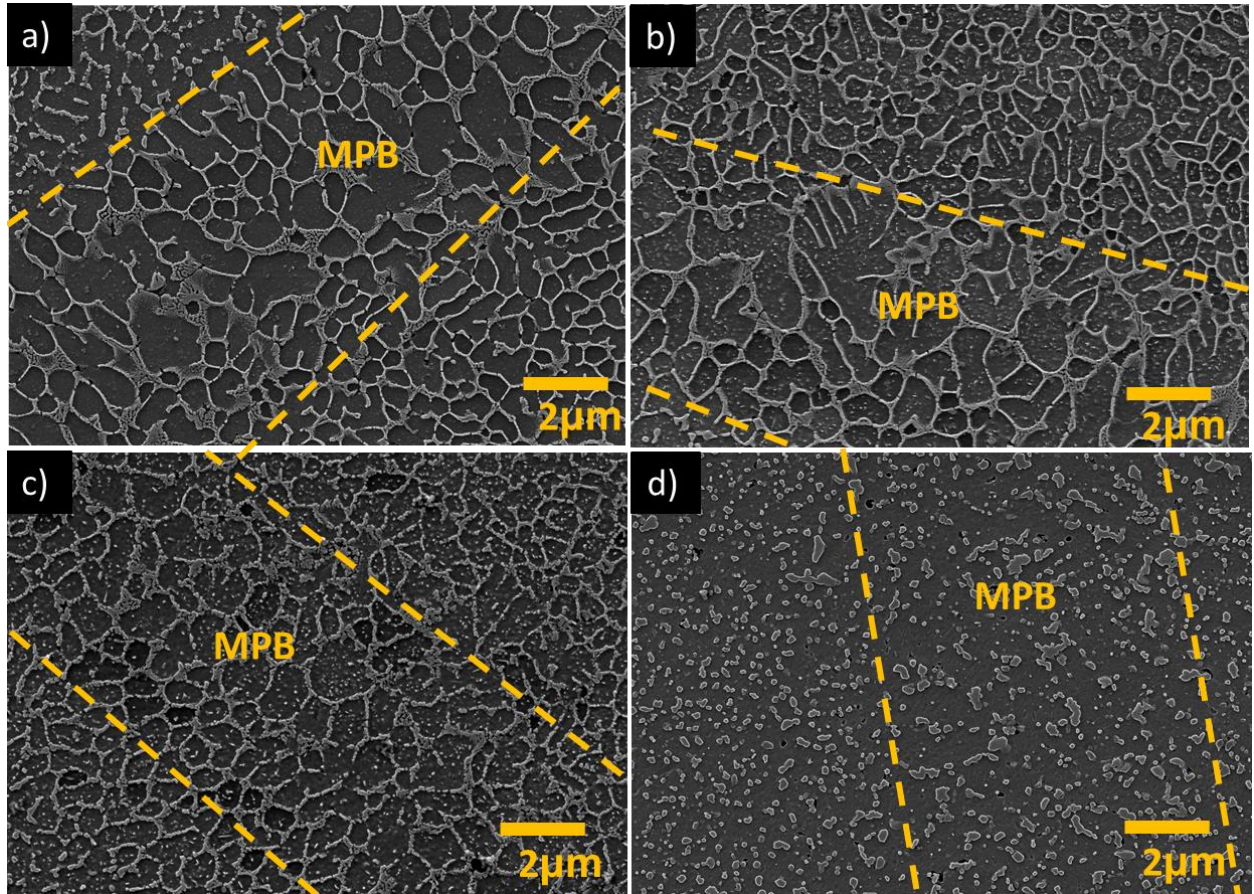

Figure 2: SEM images showing the surfaces of additive manufactured specimens. The discontinuous lines denote the presence of a melt pool border (MPB). Specimens: a) no heat

treatment (NHT), b) artificially aged at 170°C for 6h (AA170), c) stress released at 250°C for 2h (SR250) and d) stress release at 300°C for 2h (SR300).
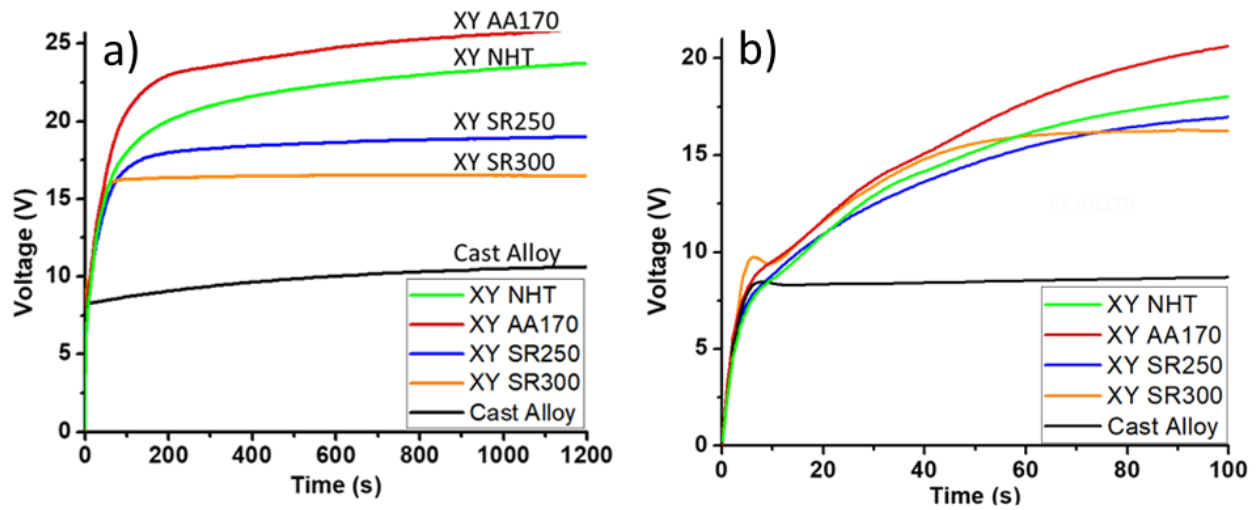
Figure 3: a) Voltage time curves of the galvanostatic anodizing of XY-AM specimens and a cast alloy (CA) as reference. b) Zoom of the first 100 seconds of the voltage-time curve.
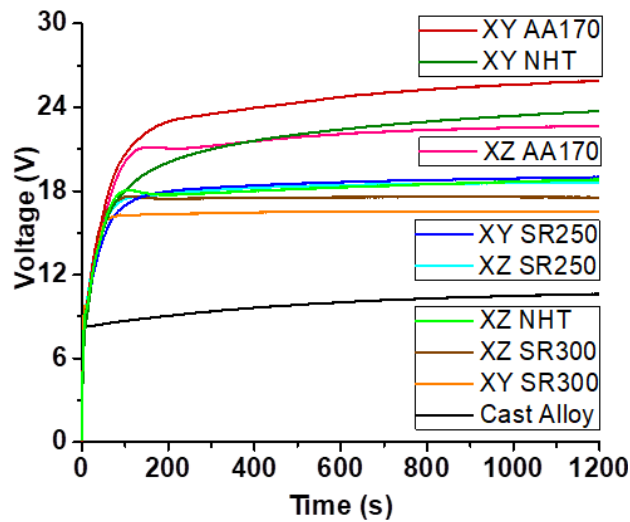
Figure 4: Voltage time curves of the galvanostatic anodizing of AM specimens and a cast alloy as reference. The differences between the XY and XZ surfaces can be observed.
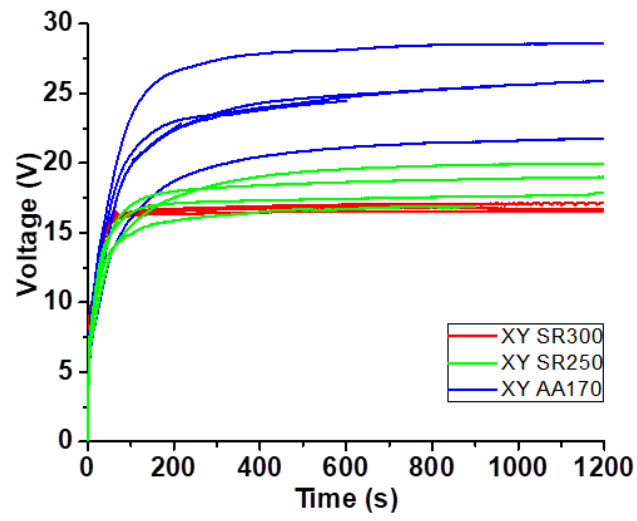
Figure 5: Collection of voltage-time curves for AA170, SR250 and SR300 specimens indicating the spread in the data for replicated experiments.
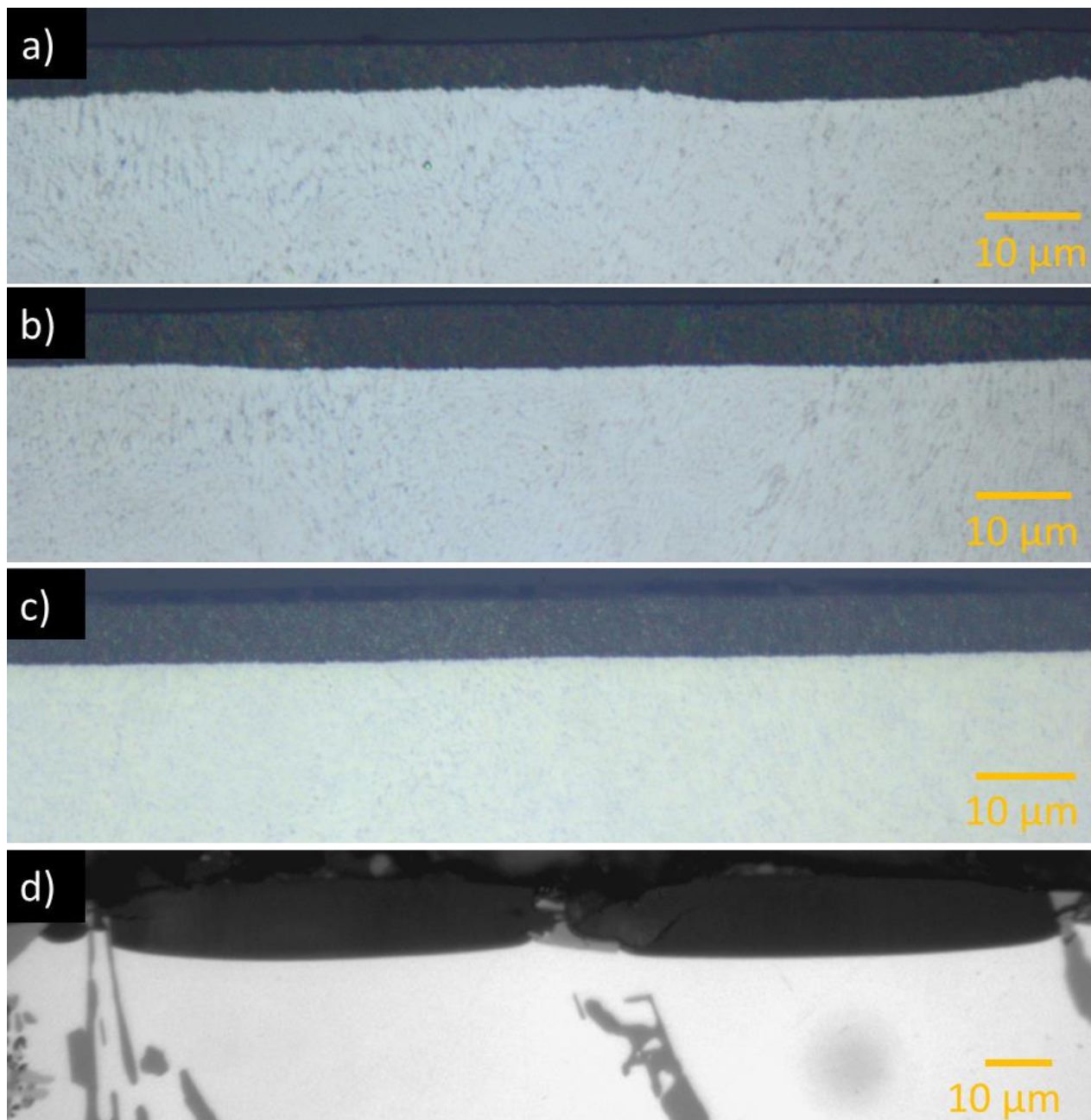
Figure 6: Optical images of the cross-section of anodized a) AA170, b) SR250, c) SR300 and d) cast alloy specimens.
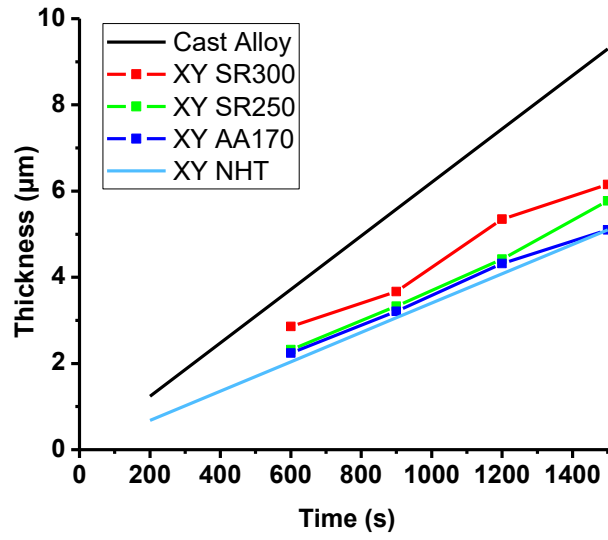
Figure 7: Evolution of thickness with anodizing time for AM specimens and a cast alloy. The values for the cast alloy and the NHT material were taken from a previous work[16] .
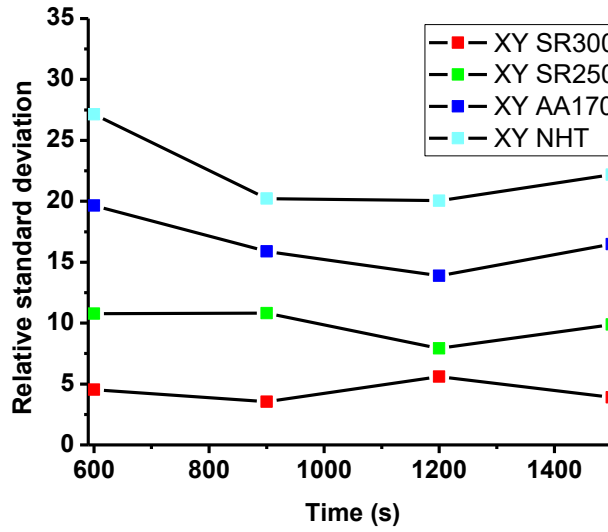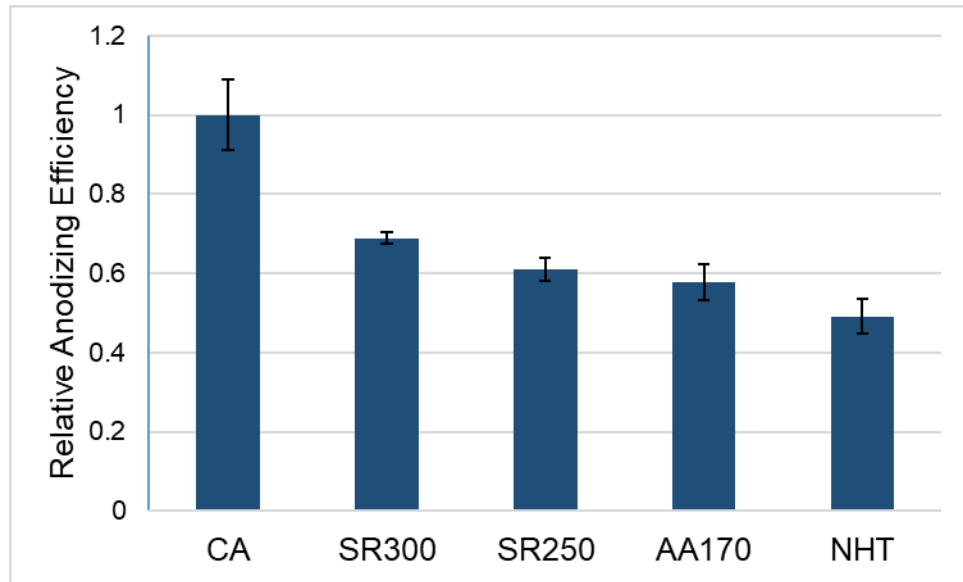

Figure 8: Relative standard deviation (RSD) for the thickness of the oxide layer for AM material having undergone various heat treatments. The RSD can be used as a measure of uniformity.

Figure 9: Relative anodizing efficiency of the additive manufactured (AM) specimens, using the cast alloy as a reference. The relative efficiency of the AM specimens gradually increases from 49% to 69% of that of the cast alloy upon application of the heat treatments.
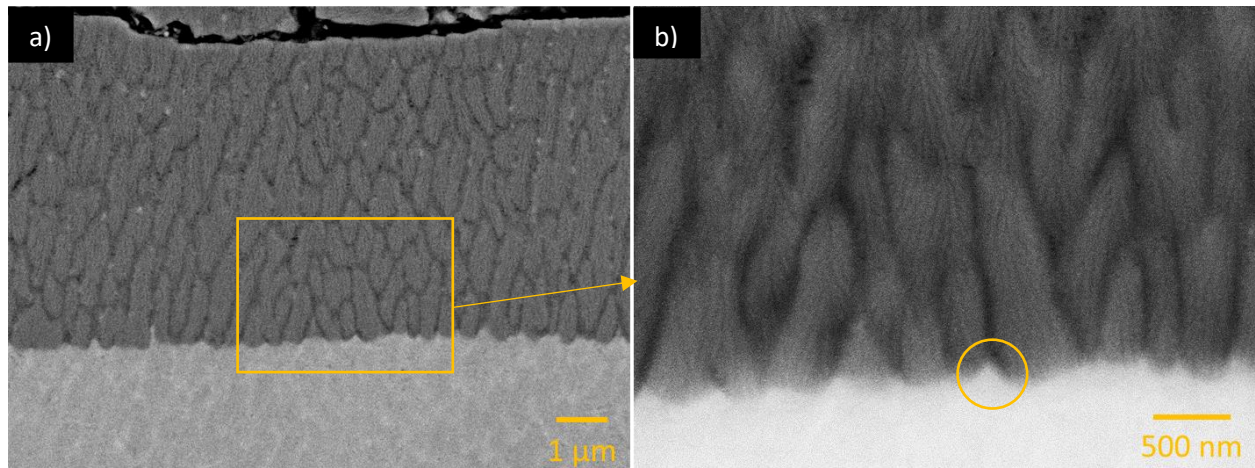
Figure 10: Backscattered electron images of the cross-section of anodized AM NHT. The oxide layer and the silicon network are clearly visible.
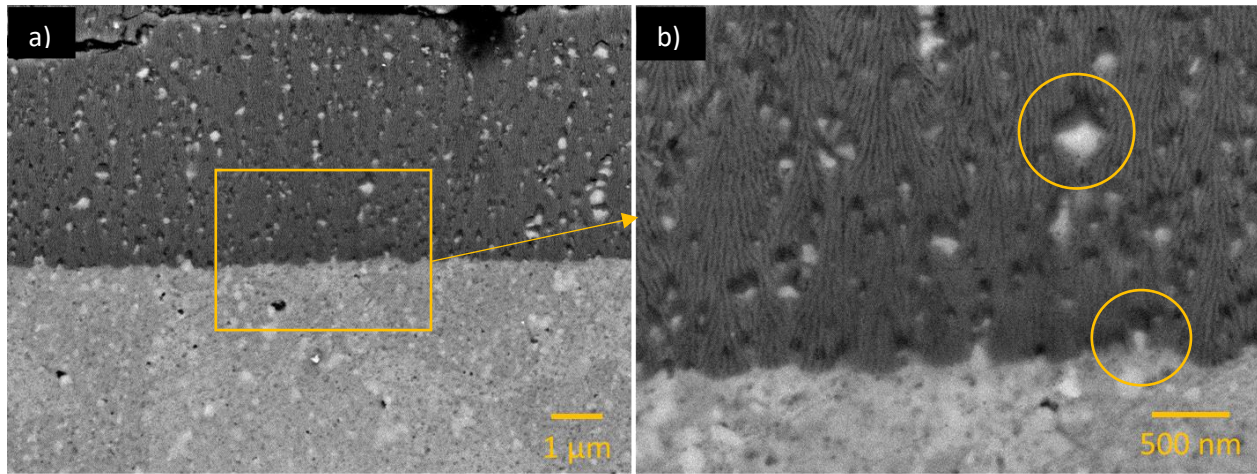
Figure 11: Backscattered electron images of the cross-section of anodized AM SR300. The oxide layer with silicon particle inclusions is clearly visible.
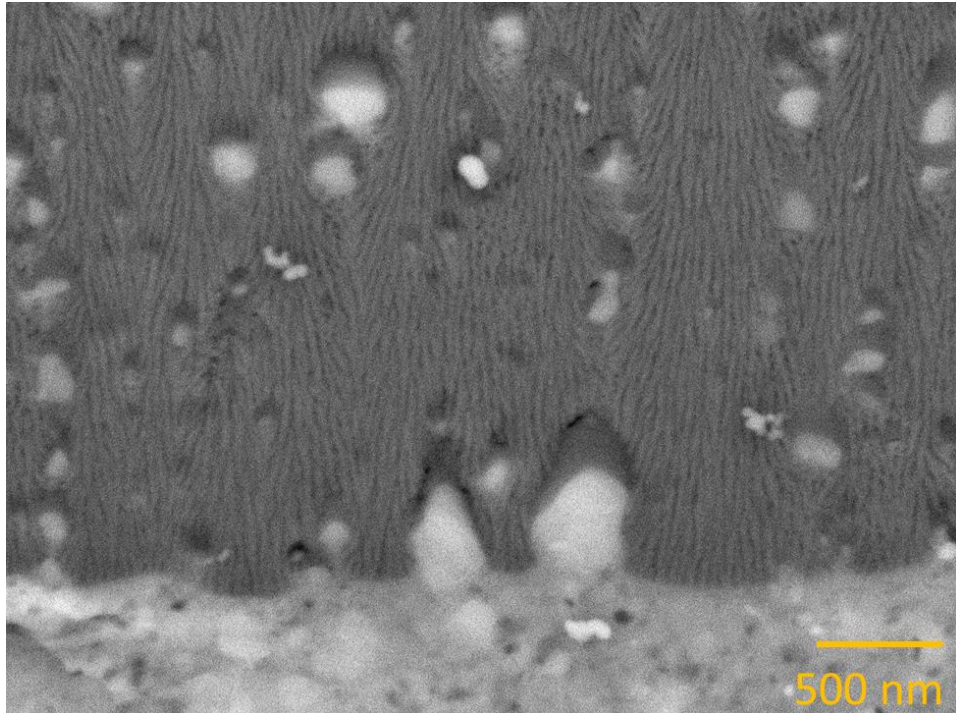
Figure 12: Higher magnification backscattered electron images of the cross-section of anodized AM SR300. Partially oxidized silicon particles with some cavities are visible.